



Framework for Multifidelity Aeroelastic Vehicle Design Optimization

Dean E. Bryson* and Markus P. Rumpfkeil†

University of Dayton, Dayton, Ohio, 45469, USA

and

Ryan J. Durscher‡

Air Force Research Laboratory, Aerospace Systems Directorate, Wright-Patterson AFB, Ohio, 45433, USA

A multifidelity aeroelastic analysis has been implemented for design optimization of a lambda wing vehicle. The goal of the multifidelity, multidisciplinary approach is to capture the effects of nonlinear, coupled phenomena on vehicle performance at a cost amenable to conceptual and preliminary design. The goal of the optimization is to maximize range at a supersonic flight condition under constraints on trim, wing deformation, and structural stresses. The design variables include planform shape, material gauges, and cruise angle of attack. The low-fidelity model couples linear, finite-element structural analysis with linear panel aerodynamics. The high-fidelity model couples structural modes with Euler computational fluid dynamics. A single, unified geometric representation is central to the multifidelity, multidisciplinary process, ensuring compatibility between disciplines and fidelities. Finite differences are used to calculate coupled, aeroelastic gradients. Good sensitivities are obtained for the low-fidelity model. However, noise in the high-fidelity response is found to dominate some derivatives, and is an area for further work. The optimization is demonstrated using the low-fidelity simulation, motivating the use of multifidelity techniques to reduce the cost of high-fidelity optimization.

Nomenclature

C	Vehicle fuel consumption
C_D	Vehicle drag coefficient
C_L	Vehicle lift coefficient
C_M^{cg}	Vehicle pitching moment coefficient about the center of gravity
f	Optimization objective function
g	Optimization inequality constraint
h	Optimization equality constraint
q	Dynamic pressure
R	Vehicle range
S	Vehicle planform area
V	Vehicle velocity
W_c	Vehicle nominal cruise weight
W_i	Vehicle initial weight
W_f	Vehicle final weight
ρ	Kreisselmeier-Steinhausen weighting parameter
σ	Structural stresses

*Ph.D. Candidate, Dept. of Mechanical and Aerospace Engineering, brysond1@udayton.edu, Member AIAA

†Associate Professor, Dept. of Mech. and Aerospace Engineering, Markus.Rumpfkeil@udayton.edu, Senior Member AIAA

‡Research Engineer, Aerospace Vehicles Division, Member AIAA

I. Introduction

Traditional aircraft design in the conceptual and preliminary phases is based largely on historical data and low-fidelity modeling. This approach is necessitated by the large number of configurations to be evaluated, the speed and cost of higher-fidelity predictions, and the level of detail to which the vehicle has been defined. However, these analyses, which are generally performed without inter-disciplinary couplings, may fail to accurately predict vehicle performance, leading to missed opportunities for improvement as well as cost and schedule overruns to correct defects discovered late in design.¹ Furthermore, decisions made prior to the milestone of down-selecting a vehicle concept drive three-quarters of an aircraft system's life cycle cost² while design freedom diminishes quickly.

Multifidelity design methods seek to address these issues by balancing the cost and accuracy of predicting vehicle performance. Lower-fidelity data may predict the overall trend of the design space and identify promising regions, while higher-fidelity data provide a basis for correcting inaccuracies. These calibrations typically implement surrogate models, such as polynomial expansions or kriging, that capture varying degrees of non-linearity in the error between high and low fidelity. Identifying cases where the calibration process becomes inadequate remains a challenge. The trust region optimization framework³ is a popular approach to addressing this need. This methodology constrains the use of approximate models to a local region where the corrected low-fidelity data is believed to be adequate. The size of this region is adjusted heuristically based on the error between the approximate and true high-fidelity function.

This paper considers the optimal design of a lambda wing vehicle to maximize its range. The aeroelastic vehicle deformation will be included to provide a more complete picture of performance, and multifidelity methods will be used to provide high-fidelity predictions accelerated by leveraging low-fidelity data. The lambda wing planform strives to balance sub- and supersonic performance. Initially, to demonstrate the optimization framework, the vehicle will be optimized for supersonic conditions only. While the multidisciplinary couplings here are limited to aeroelasticity, the design methods are extensible to include other disciplines such as propulsion as well as stability and control.

II. Methodology

II.A. Optimization Problem Definition

The baseline lambda wing vehicle configuration is depicted in Figure 1. To maximize the vehicle range, a preliminary design-level optimization is performed using static aeroelastic analyses. The multidisciplinary problem includes the planform geometry and structural gauges. The highest fidelity considered consists of body-fitted Euler Computational Fluid Dynamics (CFD) coupled with linear structural mode shapes. The lowest fidelity implements panel aerodynamics tightly coupled with full, linear structural Finite Element Analysis (FEA).

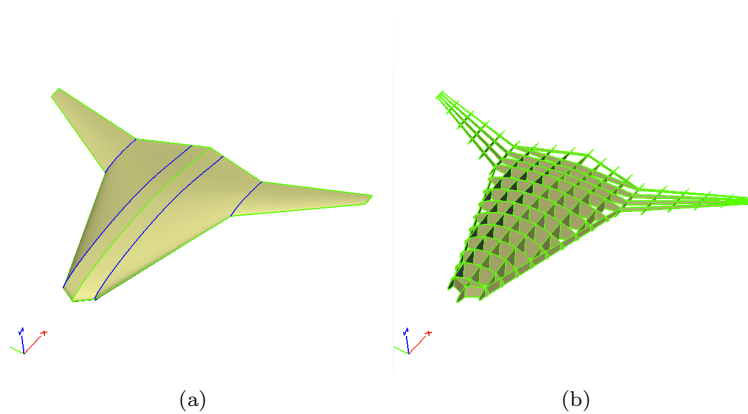


Figure 1. Outer mold line and internal layout of the baseline lambda wing vehicle.

The aircraft range may be calculated using the Breguet range equation,

$$R = \frac{V}{C} \frac{C_L}{C_D} \ln \frac{W_i}{W_f}. \quad (1)$$

The lambda wing planform design seeks to balance subsonic and supersonic performance. As a preliminary simplification, the optimization is only considered here at Mach 1.2. A constant engine performance assumption further simplifies the problem. Thus, by rearranging Equation (1) and taking its negative, the objective function to minimize becomes

$$f = -\frac{RC}{V} = \frac{C_L}{C_D} \ln \frac{W_f}{W_i}. \quad (2)$$

For this study, it is assumed that gross take-off mass is constant at 23000 kg based on data taken from Alyanak *et al.*⁴ This assumption is enforced between different configurations by varying the fuel weight. The aerodynamic performance is driven by the vehicle outer mold line coupled with the aeroelastic deformations, while the weight performance is driven by the structures discipline. The vehicle weight at the end of cruise W_f equals the weight of subsystems (estimated by textbook methods), payload, and structure.

The optimal designs must satisfy several constraints to be valid. First, the vehicle must trim. At the most basic level, the lift must equal the aircraft weight at the nominal design condition,

$$h_1 = \frac{qSC_L}{W_c} - 1 = 0. \quad (3)$$

As a simplification to the aeroelastic analysis problem, the vehicle is defined without control surfaces, which would be used to trim the moments. For the design optimization, the resultant moments will be monitored but not constrained.

The structure must bear the applied loads without failing. On an element-by-element basis, these constraints may be defined based on von Mises stresses σ_{VM} and failure stresses σ_F ,

$$\frac{\sigma_{VM,i}}{\sigma_{F,i}} - 1 \leq 0. \quad (4)$$

However, this implementation introduces a large number of constraints. Using an aggregation technique such as the Kreisselmeier-Steinhauser (KS) function^{5,6} reduces the burden on the optimizer by combining stress constraints over patches of structural elements (such as regions of constant thickness skin or spars). The aggregated inequality constraints are defined as

$$g_j = \frac{1}{\rho} \ln \sum_{i=1}^{N_{elem}} e^{\rho \left(\frac{\sigma_{VM,i}}{\sigma_{F,i}} - 1 \right)} \leq 0. \quad (5)$$

In the absence of aeroelastic divergence analysis, constraints on the wing deflection are also prudent. Limiting the magnitude of the tip displacement, the constraint is expressed as

$$g_k(X) = \frac{\|\delta_{tip}(X)\|_2}{\delta_{lim}} - 1 \leq 0. \quad (6)$$

The structural design variables may be defined under varying levels of assumptions to reduce the size of the optimization problem. At the most detailed level, the upper and lower skins would have separate material gauges, and would be further segmented into spanwise patches delineated by ribs. The wing spars would exhibit a similar stepwise taper. The outboard wing ribs have uniform gauges, as do the inboard bulkheads, ribs, and kick spars.

However, to reduce the size of the design problem for this initial demonstration, the skin gauges are symmetric on upper and lower surfaces, and are constant on three spanwise patches demarcated by the leading edge breaks. The material gauges of the internal structure are also separated into patches. The spar gauges are constant over two separate patches, the outboard wing and the centerbody, as are the ribs. The centerbody bulkheads also have a uniform gauge.

To design the planform, the area is assumed to be constant at 230 m² for the full vehicle, again based on data from Alyanak *et al.*^{4,7} The free design variables considered include aspect ratio, outboard sweep angle, and outboard taper ratio. The aspect ratio is a primary driver of the induced drag and structural weight.

The outboard sweep angle is expected to have a significant impact on wave drag. The centerbody is held constant for packaging considerations, though the sweep angle of the midboard leading edge varies slightly as the chord of the outboard wing varies.

From an overall vehicle perspective, the angle of attack is a design variable free to satisfy the trim condition.

In summary, the reduced-size optimization problem is formally defined as:

$$\begin{aligned}
 & \text{minimize} && f(X) = \frac{C_L(X)}{C_D(X)} \ln \left(\frac{W_f(X)}{W_i} \right) \\
 & \text{with respect to} && X = [\alpha, AR, \Lambda_{out}, \lambda_{out}, t_{skin}, t_{spar}, t_{rib}] \\
 & \text{subject to} && h_1(X) = \frac{qSC_L(X)}{W_c} - 1 = 0 \\
 & && g_1(X) = \frac{1}{\rho} \ln \sum_{i=1}^{N_{skins}} e^{\rho \left(\frac{\sigma_{VM,i}(X)}{\sigma_{F,i}} - 1 \right)} \leq 0 \\
 & && g_2(X) = \frac{1}{\rho} \ln \sum_{i=1}^{N_{spars}} e^{\rho \left(\frac{\sigma_{VM,i}(X)}{\sigma_{F,i}} - 1 \right)} \leq 0 \\
 & && g_3(X) = \frac{1}{\rho} \ln \sum_{i=1}^{N_{ribs}} e^{\rho \left(\frac{\sigma_{VM,i}(X)}{\sigma_{F,i}} - 1 \right)} \leq 0 \\
 & && g_4(X) = \frac{\|\delta_{tip}(X)\|_2}{\delta_{lim}} - 1 \leq 0 \\
 & && x_i^L \leq x_i \leq x_i^U
 \end{aligned} \tag{7}$$

The multifidelity optimizer currently implemented, as described in Section II.B.4, is an unconstrained optimization algorithm. Thus, to introduce the constraints into the problem, a quadratic penalty function is used

$$\tilde{f}(X) = f(X) + w_{h_1} h_1^2(X) + \sum_{i=1}^4 w_{g_i} \max(g_i(X), 0)^2. \tag{8}$$

The penalty weights were selected based on the relative magnitudes of the responses at the baseline configuration, and different weighting schemes are compared in Section III.B. The design variable bounds are provided in Table 1. Note that the aspect ratio variable seems very limited, however, because the entire lifting body is included in the reference area, the variable produces spans ranging from 10 to 30 m.

Table 1. Design variable bounds.

Variable	Lower Bound	Upper Bound	Units
Angle of Attack α	-5	5	degree
Aspect Ratio AR	2	4	—
Sweep Λ	35	60	degree
Taper Ratio λ	0.2	0.5	—
Skin Gauge t_{skin}	0.005	0.05	m
Spar Gauge t_{spar}	0.005	0.05	m
Rib Gauge t_{rib}	0.005	0.05	m

II.B. Multifidelity, Multidisciplinary Analysis

The responses for the optimization problem defined above are calculated from the multifidelity, multidisciplinary analysis depicted in Figure 2. The process begins with the selection of design variables via an optimizer, parametric study, or other means. The model configuration and geometry generator, Computational Aircraft Prototype Syntheses (CAPS),⁸ interprets the parameters into the required aerodynamic and structural analysis models. These models feed the subsequent disciplinary analyses.

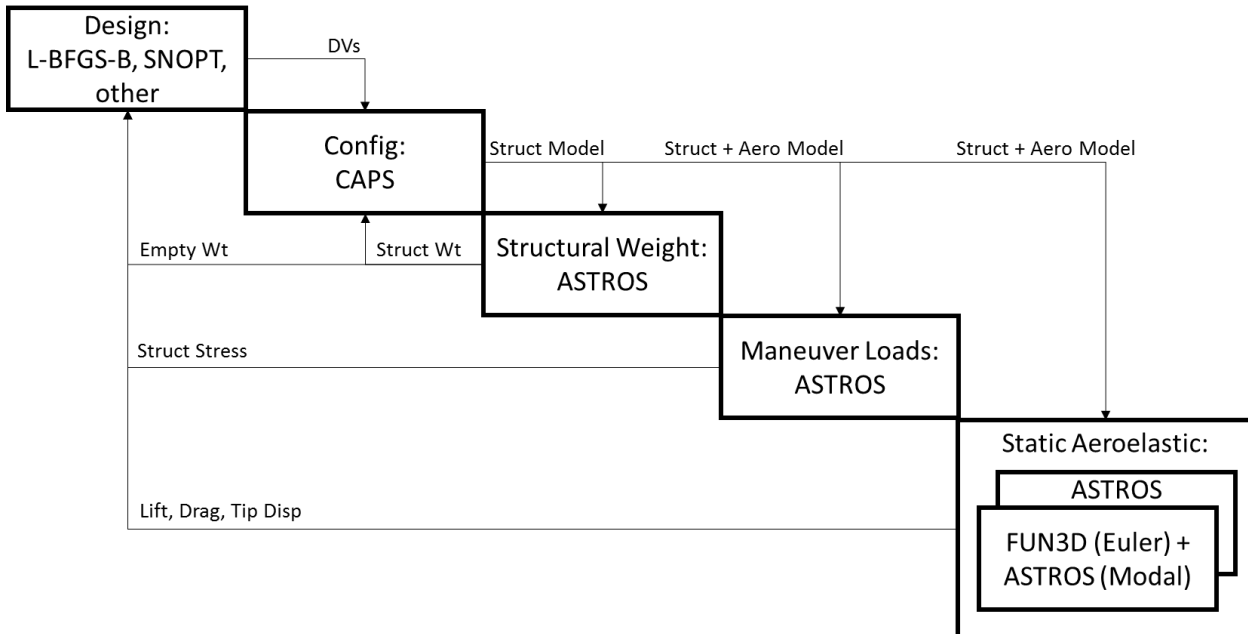


Figure 2. Logical connections and fidelities in multifidelity, multidisciplinary analysis.

The first analysis is the evaluation of the structural weights of the as-designed model using the Automated STRuctural Optimization System (ASTROS).^{9,10} At this point, it is reemphasized that the gross takeoff weight is defined to be constant across all configurations. The structural weights combine with fixed estimates of subsystem weights yield the empty weight used in the range calculation. The margin between takeoff and empty weights indicates the available fuel weight, of which 50% is used for the design maneuver and trim weight.

The structural analysis model is updated to reflect this design weight before running the maneuver loads analysis in ASTROS. This analysis determines the stresses and strains for the structural constraints by trimming (angle of attack only) the vehicle to achieve a prescribed load factor. Since the simplifying assumption is made that the upper and lower skins have the same material gauges, a 9-g pull-up maneuver is sufficient for the analysis.

The same structural analysis model also feeds the subsequent multifidelity static aeroelastic evaluation. All fidelities implemented are required to produce lift, drag, and tip displacement, which will be used in the objective and constraint evaluations. The lowest fidelity considered is ASTROS, which combines linear FEA with panel aerodynamics. It generates structural deformations, lift, and induced drag. The code AWAVE,¹¹ which is a low-order code that estimates wave drag, was considered to produce a more complete drag estimate. However, parametric studies indicated that the predictions by AWAVE are too noisy to be useful in the optimization. The highest fidelity considered is Fully Unstructured Navier-Stokes 3D (FUN3D)^{12,13} in Euler mode with modal structures calculated again by ASTROS. The loads transfer and mesh deformation are handled internally by FUN3D.

The aeroelastic optimization requires coupled gradients of the response functions. ASTROS already provides sensitivities of responses with respect to the material gauges, and FUN3D provides rigid aerodynamic sensitivities with respect to shape parameters. However the efficient calculation of coupled gradients is a topic of ongoing research. Here, finite differences are used as a demonstration. More efficient and accurate methods will be considered as the tools become available.

II.B.1. Parametric Geometry and Analysis Model Generation

A shared geometric representation of the vehicle is central to the multifidelity, multidisciplinary analysis and optimization. Using a single source ensures that the inputs given to each analysis are consistent and aids in the transfer of data between disciplines. This objective is achieved using CAPS.⁸

Within CAPS exists a parametric, attributed model of the lambda wing vehicle. The attributes provide

logical information required for the generation of analysis inputs. For example, attributes identify the vehicle skins where aeroelastic data transfers take place, symmetry planes for the application of boundary conditions, and bodies to which material properties should be applied. When a design parameter is changed, the geometry is regenerated, and analysis models (meshes, properties, etc.) may be requested for various disciplinary analyses. At the time of writing, analyses demonstrated include structural FEA using two-dimensional elements and aerodynamics from empirical methods, through panel methods, up to Navier-Stokes.

The analysis model generation proceeds as follows. Using the current design parameters, the airfoil cross-sections and the planform shape are determined. Lofting these airfoils provides a solid body representing the outer mold line (OML). These same airfoils also provide the boundaries for defining mid-surface aerodynamic panel models. The CFD domain is generated by subtracting the OML solid from a bounding box.

The internal structure results from intersecting the OML body with a grid representing the structural layout. The layout may have variable topology, though here the topology is held constant, and the shape follows the planform parameterization. The wing skins are extracted from the outer surface of the OML body. Sample geometric entities used for building the analysis models are presented in Figure 3.

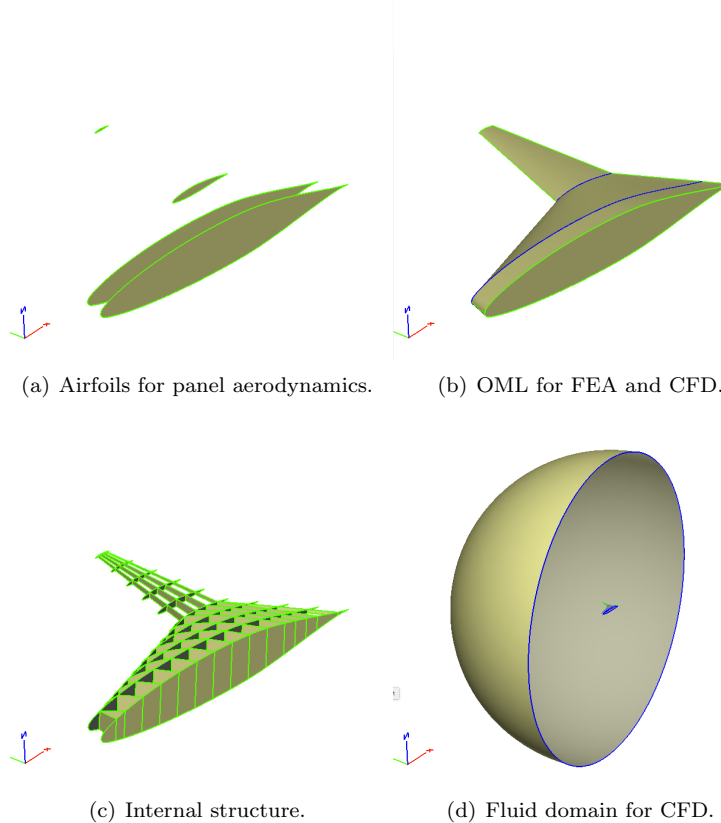


Figure 3. Representations of the same vehicle model with different geometric fidelities for multidisciplinary analyses. Size of CFD volume is reduced for illustrative purposes.

II.B.2. Low-Fidelity Aeroelastic Modeling

The low-fidelity analysis is performed with the ASTROS^{9,10} package. ASTROS performs static, modal, and transient linear FEA, and has an internal aerodynamics capability for static and dynamic aeroelastic analyses. The aerodynamics model, Unified Subsonic and Supersonic Aerodynamic Analysis (USSAERO),¹⁴ generates pressures based on the superposition of sources and vortices over a panel representation of the vehicle. USSAERO simulates both lifting surfaces and non-lifting bodies, though the latter capability is not required for the current configuration. The transfer of loads and displacements between the two disciplines is handled using surface splines.¹⁵

The optimization utilizes the ASTROS static aeroelastic capability, specifying the angle of attack, vehicle

shape, and structural gauges, and receiving the vehicle weight, finite element stresses and displacements, and lift and induced drag coefficients. A mesh convergence study for the aeroelastic cruise prediction is presented in Table 2 for three different vehicle configurations. With the first configuration being the baseline, the second configuration reduces the aspect ratio, increases sweep, and thickens the structure with the goal of creating a very stiff wing. The third configuration, in contrast, increases aspect ratio and reduces the sweep and material gauges to produce a relatively flexible wing. These configurations are illustrated in Figure 4 with sample structural and fluid meshes. The models selected for the optimization have approximately 2200 nodes and 1664 aerodynamic panels for the low-fidelity simulation.

Table 2. Mesh convergence of ASTROS aeroelastic simulation. Errors are with respect to finest mesh.

FEA Nodes	Aero Panels	C_L	Error	C_D	Error
Config 1					
954	104	0.1170	3.9%	6.79E-04	4.8%
1329	416	0.1141	1.4%	6.60E-04	1.8%
2249	1664	0.1126	—	6.48E-04	—
Config 2					
1369	104	0.1835	3.1%	2.63E-03	3.0%
1375	416	0.1798	1.1%	2.58E-03	1.1%
2299	1664	0.1779	—	2.56E-03	—
Config 3					
894	104	5.97E-02	3.9%	1.47E-04	4.6%
1294	416	5.83E-02	1.5%	1.43E-04	1.9%
2234	1664	5.74E-02	—	1.41E-04	—

II.B.3. High-Fidelity Aeroelastic Modeling

The high-fidelity analysis uses the internal aeroelasticity capability¹⁶ in the NASA FUN3D code.^{12,13} The results presented here assume an inviscid fluid. FUN3D is a node-centered, implicit, upwind-differencing finite-volume solver.^{12,16} The integrated aeroelastic analysis utilizes a modal structural representation computed by an external solver, in this case ASTROS. While the coupled aeroelastic equations are implemented for transient analysis,¹⁶ here the solution is time-marched to static equilibrium. The volume mesh deformation implements a linear elastic analogy driven by the surface mesh displacements transferred from the structure.¹⁶ The initial grids are generated using AFLR^{17,18} for the surface and volume meshes. A representative mesh is provided in Figure 5.

The transfer of mode shapes from the structural mesh to the fluid surface mesh is handled by CAPS internally. The structural and fluid surfaces are matched by tagging the parametric geometry model with attributes. The nodal displacements from the structural solution are read in through an analysis interface and mapped onto the source geometry, which has knowledge of both the structural and fluid meshes. Each mode shape is then transferred to the fluid surface mesh by interpolating the displacements from the structural mesh through this shared geometry. This transfer is performed automatically with no further action required by the user.

A mesh convergence study is provided in Table 3 for the same three configurations as ASTROS. The meshes used for optimization have approximately 300,000 nodes for the CFD mesh and 2200 nodes for the FEA mesh. Eighteen mode shapes are included in the dynamic analysis. The finite element model is allowed to have rigid body motion about the wing box root to simulate free flight, though the rigid body modes are omitted from the CFD simulation. Inviscid wall boundary conditions are applied to the wing outer mold line, and the symmetry plane is modeled with a symmetric boundary condition.

The time step is selected to have twelve steps per cycle of the highest modal frequency. A maximum of twenty subiterations are used per time step, though temporal error tracking is also used. After the first time step, the subiteration sequence is truncated once the continuity residual of the mean flow falls two orders of magnitude below the estimated temporal error. However a minimum of six subiterations are used over the vast majority of time steps. The CFL number used is fifty.

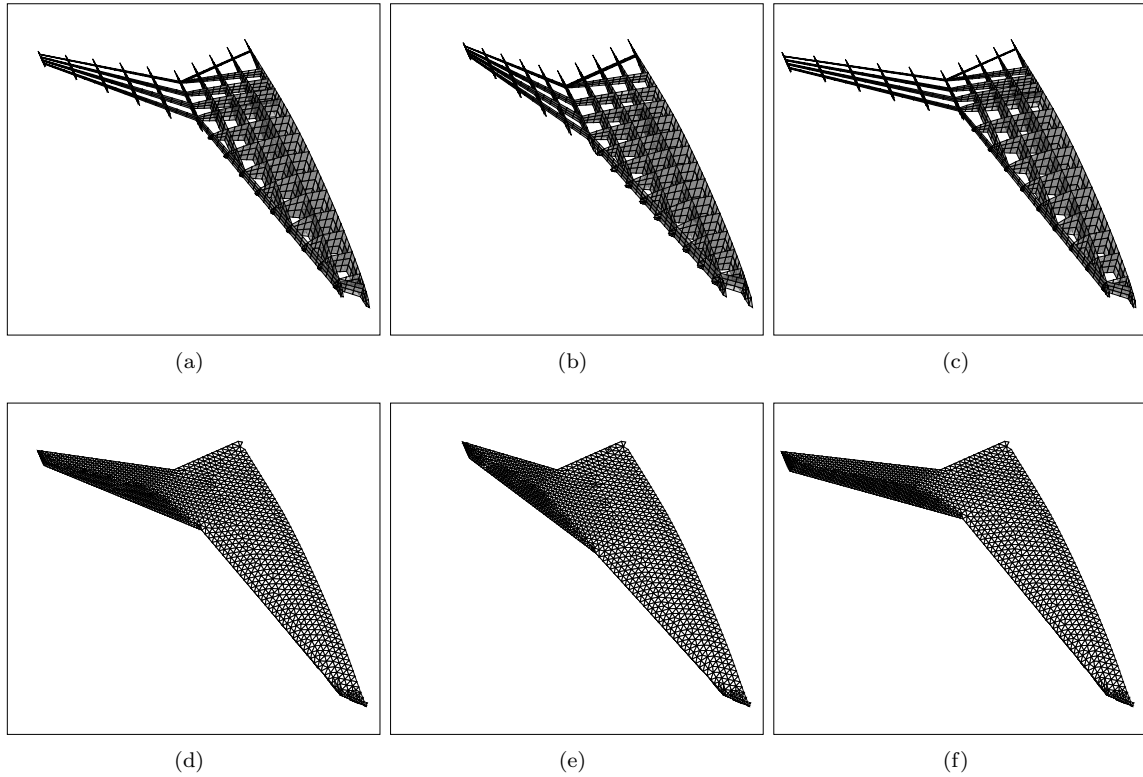


Figure 4. Automated structural and fluid meshes for three vehicle variants (top: structure with transparent skins, bottom: fluid surfaces). Coarse meshes are shown, and missing cells along the fluid mesh root are artifacts of clipping the symmetry plane for clarity.

Table 3. Mesh convergence of FUN3D+ASTROS aeroelastic simulation. Errors are with respect to finest mesh.

FEA Nodes	CFD Nodes	# Modes	Steps per Min Period	C_L	Error	C_D	Error
Config 1							
1329	70254	12	12	8.655E-02	-2.8%	3.411E-02	2.2%
2249	292385	18	24	8.834E-02	-0.78%	3.354E-02	0.51%
2249	856564	18	24	8.903E-02	—	3.337E-02	—
2249	292385	18	12	8.834E-02	-0.78%	3.354E-02	0.51%
Config 2							
1375	64441	12	12	1.327E-01	-2.8%	3.468E-02	1.2%
2299	272846	18	24	1.354E-01	-0.81%	3.429E-02	0.058%
2299	800532	18	24	1.365E-01	—	3.427E-02	—
2299	272846	18	12	1.354E-01	-0.81%	3.429E-02	0.058%
Config 3							
1294	73048	12	12	5.803E-02	-5.7%	3.495E-02	2.8%
2234	305809	18	24	6.034E-02	-2.0%	3.420E-02	0.62%
2234	898825	18	24	6.156E-02	—	3.399E-02	—
2234	305809	18	12	6.034E-02	-2.0%	3.420E-02	0.62%

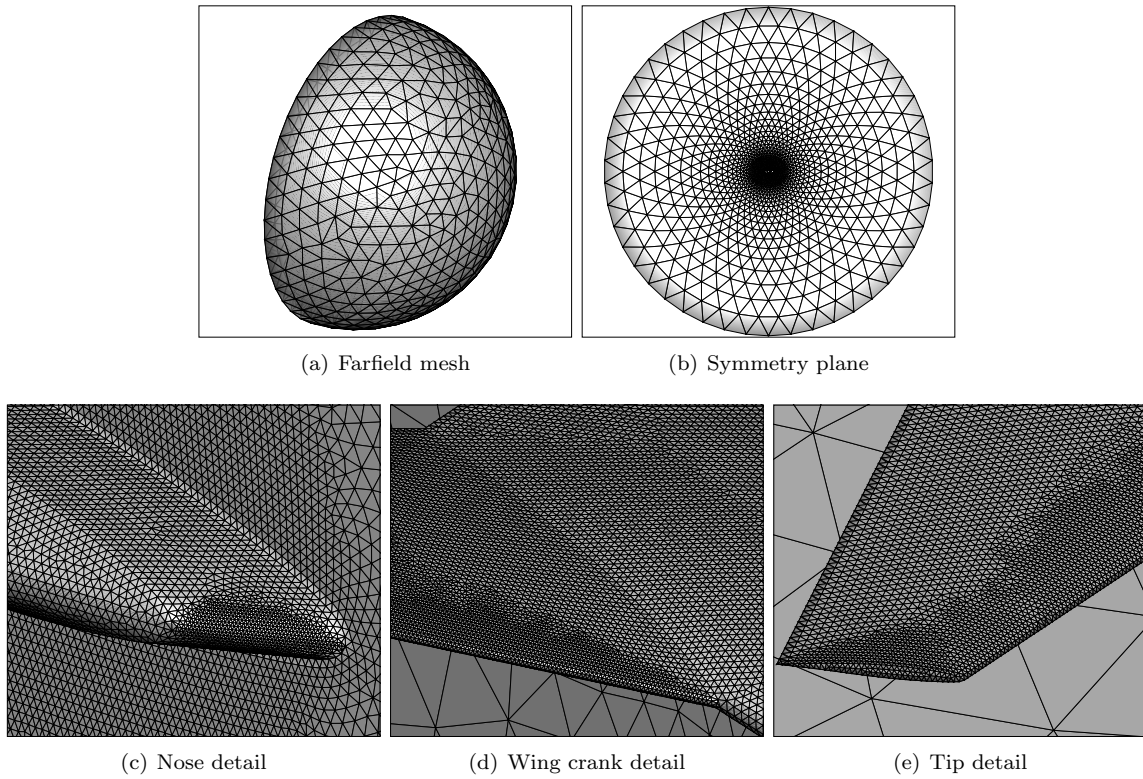


Figure 5. Representative fluid mesh.

A typical convergence history is shown in Figure 6. Because finite differences are used for gradients, the solution must be deeply converged to ensure accurate sensitivities. After a study of twenty-nine different configurations, the solution was found to be highly converged after approximately 3000 iterations.

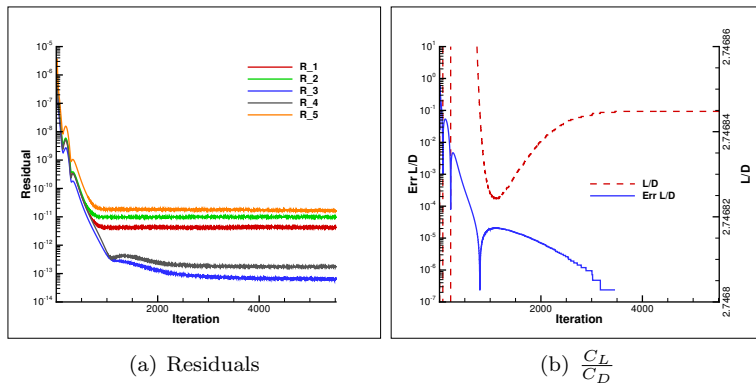


Figure 6. Typical convergence histories for aeroelastic CFD. Errors in aerodynamic coefficients are with respect to the last time step. After approximately 3500 iterations, the error vanishes to the precision of the output file.

II.B.4. Multifidelity Optimization Algorithm

The multifidelity optimization algorithm used for this design problem is the new approach of Bryson and Rumpfkeil.¹⁹ This approach is based on Trust Region Model Management (TRMM)³ with hybrid additive-multiplicative corrections (or bridge functions) to the low-fidelity analysis.^{20–22} However, the methodology adopted differs from traditional multifidelity trust region approaches in two important ways.

First, the typical approaches to hybrid bridge functions focus on finding a convex combination of individually calibrated additive and multiplicative corrections. Several strategies have been proposed for selecting the weights of the two corrections. For example, Gano, Renaud, and Sanders²³ and Ng, Huynh,

and Willcox²⁴ propose calculating the weights to force the low-fidelity model to match previously calculated high-fidelity data at a second point (in addition to the current design point), such as the previous design point or the nearest available data. In a different approach, Fischer, Grandhi, and Beran²⁵ use a Bayesian update scheme to update the weights based on data in a region surrounding the current design. Alternatively, the new approach seeks complementary corrections, which gives the surrogate model the ability to leverage multiplicative corrections where they are best used, while focusing additive corrections in other areas. Comparisons indicate that seeking complementary corrections produces superior surrogate models of the response of interest.

Second, the algorithm of Bryson and Rumpfkeil¹⁹ uses the approximate model in a different phase of optimization than the standard TRMM. TRMM implements a complete sub-optimization (multiple line searches in different directions) on the approximate model at each iteration. However, knowledge of the design space is not passed on from one iteration to the next except for the sizing of the trust region that limits use of the approximate model. This parameter is determined heuristically based on the performance of the previous approximate model relative to the true high-fidelity data. The proposed unified approach, on the other hand, utilizes the approximate model only in the line search, and determines the search direction only from high-fidelity data gathered over all the iterations, helping the optimizer to more efficiently search the design space. The unified approach still utilizes a trust region to limit the maximum allowable step size; elimination of this heuristic is a subject for future research. In addition to having memory of previous iterations, the new approach reduces the burden on the surrogate model from requiring accuracy throughout an N-dimensional hyperspace to only needing accuracy along a line through the hyperspace.

For details on the optimization algorithm and performance comparisons for analytical test functions ranging from two to twenty-five dimensions, the reader is referred to Bryson and Rumpfkeil.¹⁹

III. Results

III.A. Parametric Studies

Initially, the two aeroelastic simulations are run for a set of twenty-eight different cases; each design variable is swept through five levels, intersecting at the baseline design. A small step is taken above and below the base design, which can be used to visually verify the correctness of the finite difference gradients. Secondly, larger steps are taken to test the robustness of the simulations near the edges of the domain. Additional points are added to the sweeps of skin and rib gauges and aspect ratio to further resolve response nonlinearities and more clearly indicate the correctness of the gradient. The results of these sweeps are presented in Figures 7–11.

In addition to the variation of the responses with individual design variables, gradients calculated by finite differences are shown by vectors at the baseline design point. For the low-fidelity simulation, a step size of 10^{-3} relative to the design variable value is found to produce reliable gradients for all the design variables and responses. However, the high-fidelity model exhibits noise in the response, resulting in inaccurate sensitivities for a relative step size of 10^{-2} . These difficulties are highlighted by gradient vectors that are not tangential to the response curves in Figures 7–11. The dynamic simulations have been run out to long time horizons to ensure they are sufficiently converged to static equilibrium. Still, the noise remains, and is a topic of future investigation. A current theory is that movement of a shock on the wing, exacerbated by coupling with the modal structure, is the source.

Figure 7 shows the variation of lift coefficient for the two models. As expected the variation is linear for ASTROS, and nearly so for FUN3D over the range of angles of attack. This difference may be easily corrected by the calibrations between fidelities. The lift exhibits a hump with a maximum around aspect ratio of three, predicted by both fidelities. This hump may be indicative of an aeroelastic reversal, where the increased wing twist as angle of attack increases results in reduced lift, contrary to the expectation. This conclusion is supported by the tip displacement variation in Figure 9. The two fidelities show disagreement in the trend of lift with sweep angle and taper ratio. These differences require further investigation, but appear easily correctable by negating the ASTROS result, scaling, and adding an offset. The lift exhibits only slight variation with the structural gauges, which would be anticipated because the aeroelastic deformations are small. The greatest variation is with the skin thickness, which provides most of the bending and torsional stiffness.

Figure 8 shows the variation of drag coefficient for the two models. Again, the ASTROS prediction only includes induced drag as the AWAVE wave drag prediction was determined to be too noisy to be useful.

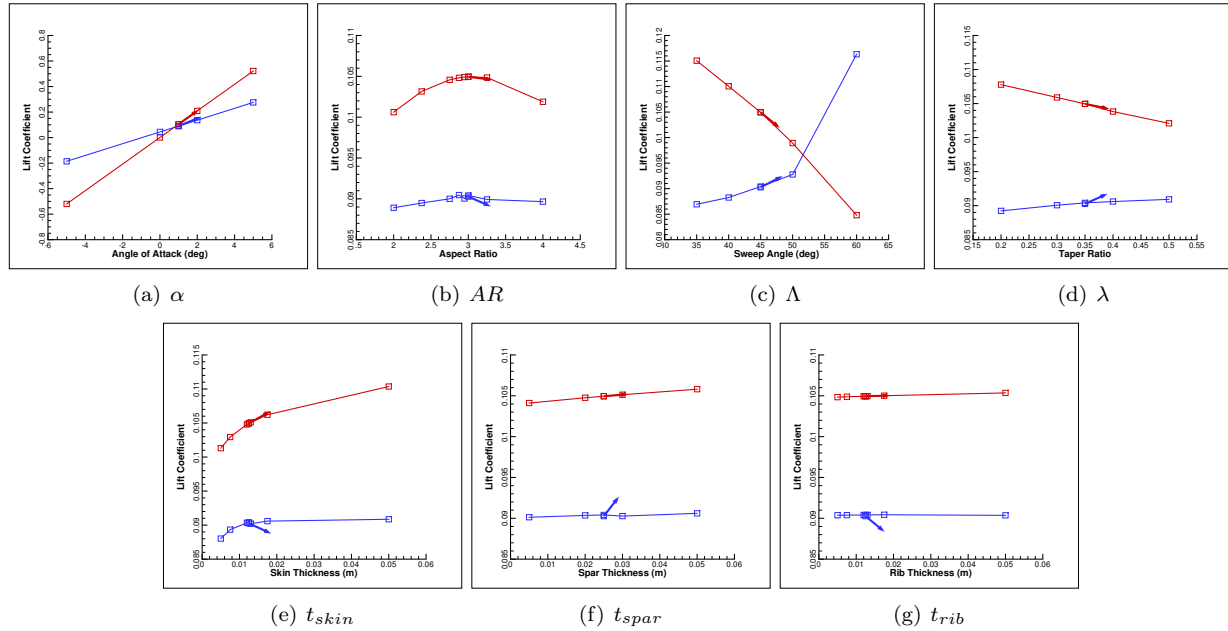


Figure 7. Comparison of lift coefficient variation with design variables for ASTROS (red) and FUN3D (blue). Vectors indicate direction of finite-difference gradient at baseline point.

Even so, the ASTROS drag follows the trend of that for FUN3D very well, differing only by a constant (i.e., the wave drag coefficient). As anticipated, FUN3D predicts decreasing drag with increasing sweep angle as the shock weakens. There is only slight variation in drag with the other parameters.

Figure 9 shows the variation of tip displacement. As expected, as skin thickness increases, the displacement decreases with ASTROS. However, FUN3D predicts a decrease initially, then an increase. This discrepancy may be an artifact of the modal model linking tip displacements with deformations nearer the root. The trends are similar between the two models for the other parameters, with the exception of angle of attack. This discrepancy may be due to the similar modal linking and requires further investigation. However, the tip displacements are small relative to the chord, and the displacement constraint is likely to be inactive in most cases. Furthermore, this constraint is only used to protect the optimizer from regions of the design space where the wing may be aero-elastically unstable.

The KS functions for the stress constraints are plotted in Figure 10. The stress constraints show no variation with angle of attack. This result is expected because the stress analysis determines a trim angle of attack to produce a pull-up. Hence, the angle of attack in the stress analysis is independent of the prescribed cruise angle. As anticipated, the stresses increase with aspect ratio due to larger bending moments for longer spans. Similarly, as the wing is swept aft, the wing becomes slightly elongated along the spar, resulting in larger bending moments and stresses. As taper ratio increases (i.e., the tip becomes larger), more load is shifted outboard, again increasing bending moments. Finally, as expected, as the structural gauges are increased, the stresses decrease as there is more material to carry the load.

The variation of vehicle empty mass is depicted in Figure 11. As expected, the mass does not change with angle of attack. As aspect ratio and taper ratio increase, the empty mass decreases by a small amount. This is due to slight variations in the center body at the outboard wing joint. To maintain constant area, the midboard sweep angle and chord length adjust by a small amount. These small changes ripple over a large area of the centerbody where the vehicle is comparatively thick. Thus small reductions in chord length at the joint lead to reductions in structural mass. In contrast, sweeping the outboard wing does not change the centerbody planform. As the wing sweeps aft, it elongates slightly, increasing mass. As anticipated, mass increases as the structural gauges increase.

III.B. Optimization

Results of preliminary optimizations using the low-fidelity function alone are presented in Figures 12 and 13. As mentioned previously, accurate high-fidelity finite differences have not been established, so optimiza-

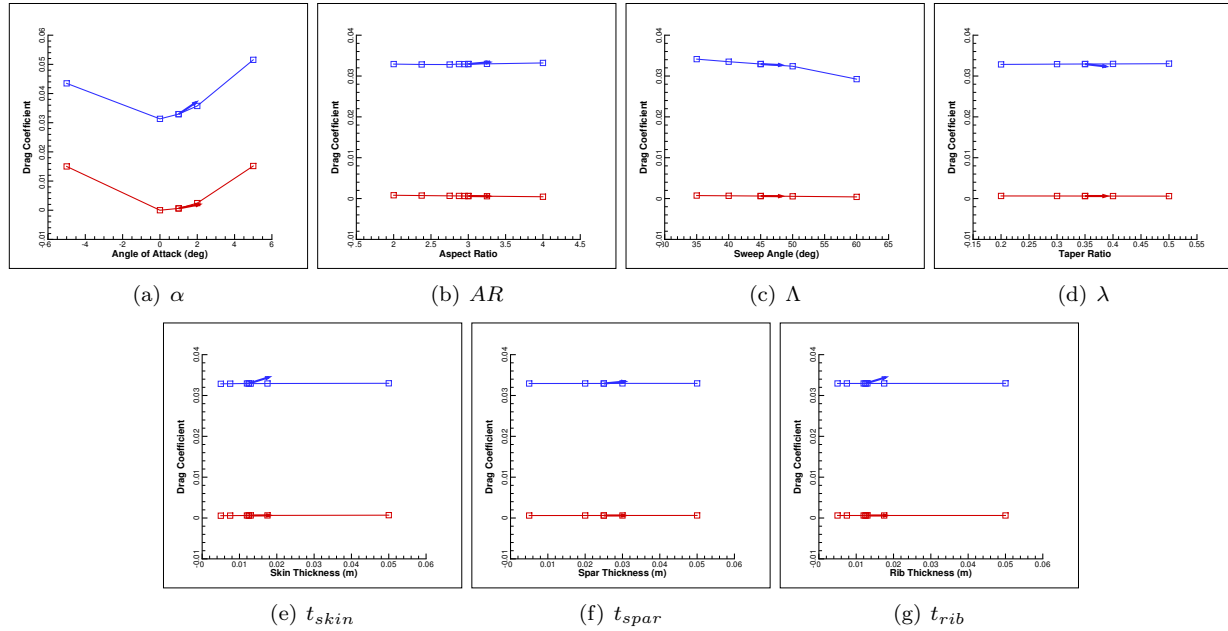


Figure 8. Comparison of drag coefficient variation with design variables for ASTROS (red; induced drag only) and FUN3D (blue). Vectors indicate direction of finite-difference gradient at baseline point.

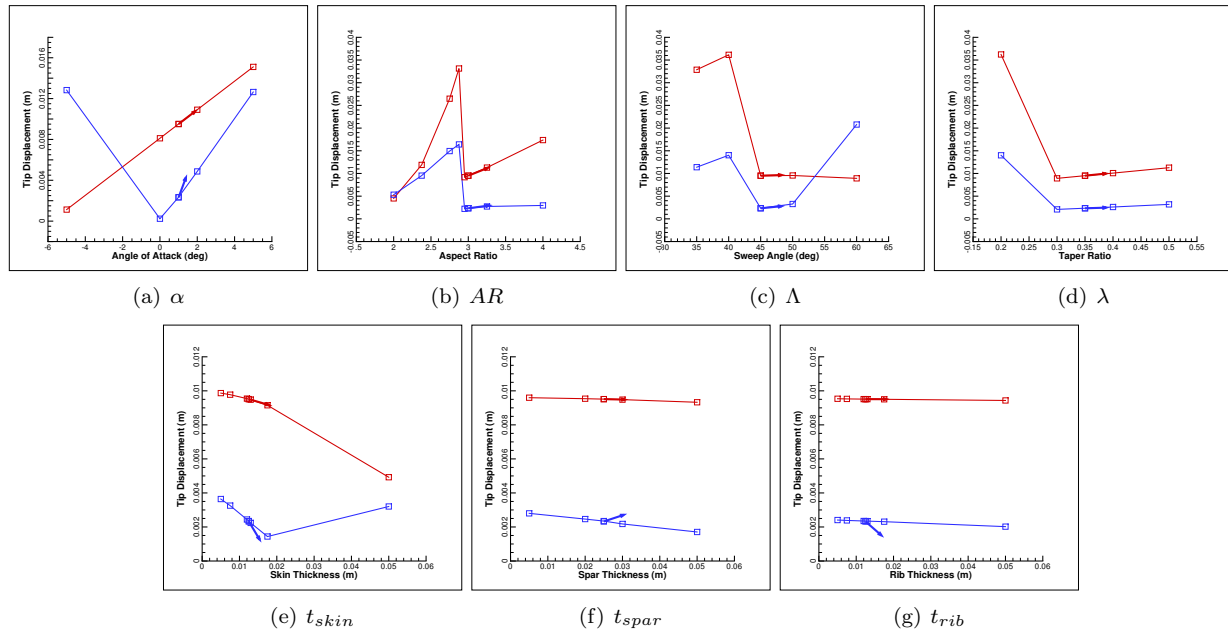


Figure 9. Comparison of tip displacement variation with design variables for ASTROS (red) and FUN3D (blue). Vectors indicate direction of finite-difference gradient at baseline point.

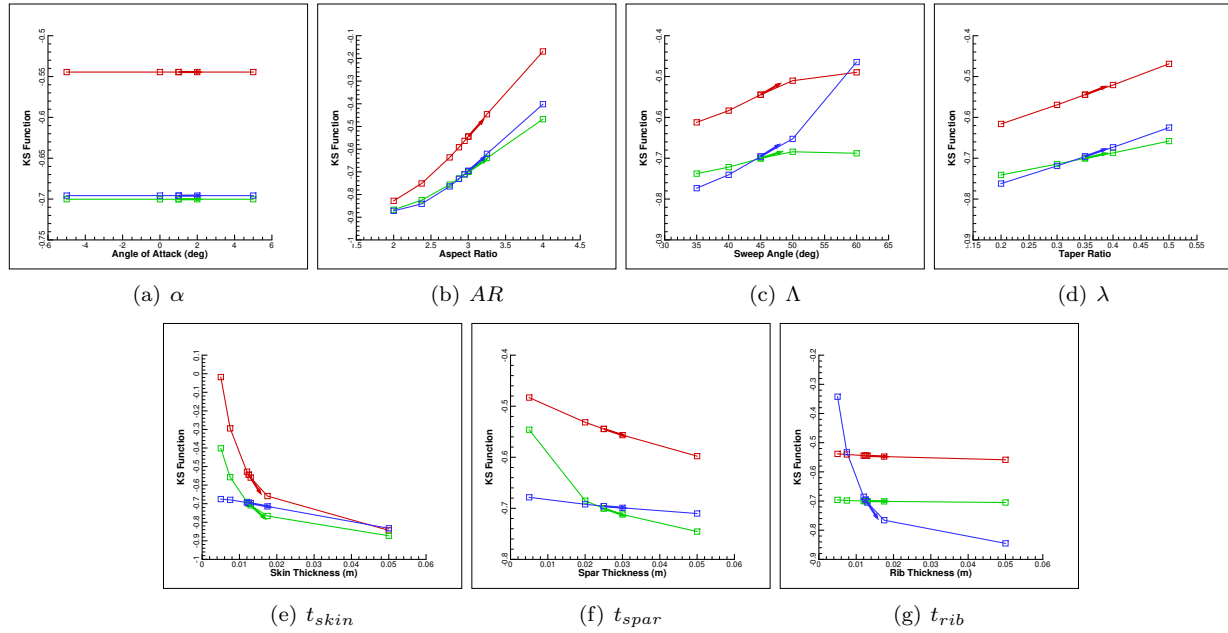


Figure 10. Variation of stress constraint KS functions with design variables (skin constraint—red, spar—green, rib—blue). Vectors indicate direction of finite-difference gradient at baseline point.

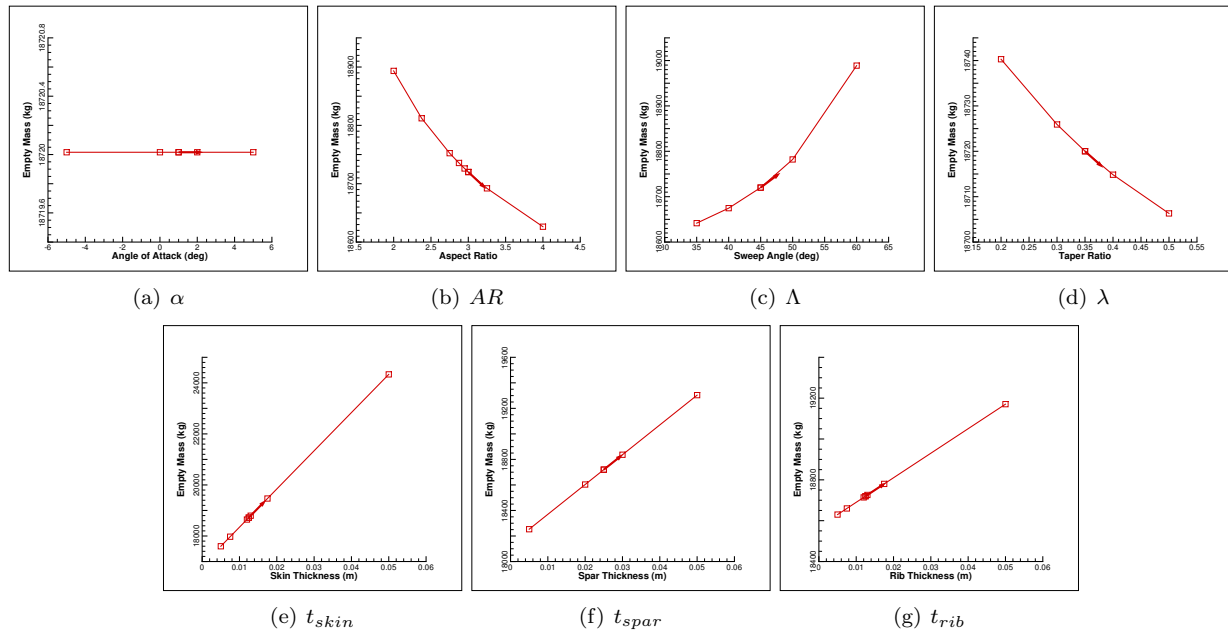


Figure 11. Variation of vehicle empty mass with design variables. Vectors indicate direction of finite-difference gradient at baseline point.

tion using the high-fidelity simulation is left for future work. For optimization with a single fidelity, the multifidelity optimizer simplifies to the BFGS quasi-Newton algorithm of Byrd, Lu, and Nocedal.²⁶ Two different constraint penalty weightings are used. For the first function, the trim constraint is weighted by a factor of 10, whereas in the second it is weighted by a factor of 1. In both cases, the range objective and displacement constraints are weighted factors of 1, and the stress constraints are weighted by a factor of 10. The reasoning behind the larger weightings is that these constraints have bearing on the physical validity of the solution, and minimal constraint violations are sought in the optimal solution. The displacement constraint, on the other hand, is introduced solely to prevent the optimizer from searching in regions where the solution may diverge, either aero-elastically or numerically. Thus, larger deviations beyond the limit are physically acceptable. The trim weighting was varied between the two functions in an attempt to provide the optimizer with more freedom to explore the design space without the narrow limits enforced by the trim constraint. Ultimately, the second penalty function with the less-restrictive trim weighting produced a better design. The geometry of the two results are compared to the initial design in Figure 14.

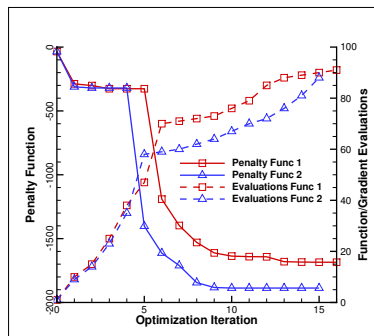


Figure 12. Comparison of convergence histories and function/gradient calls required for two penalty function weightings

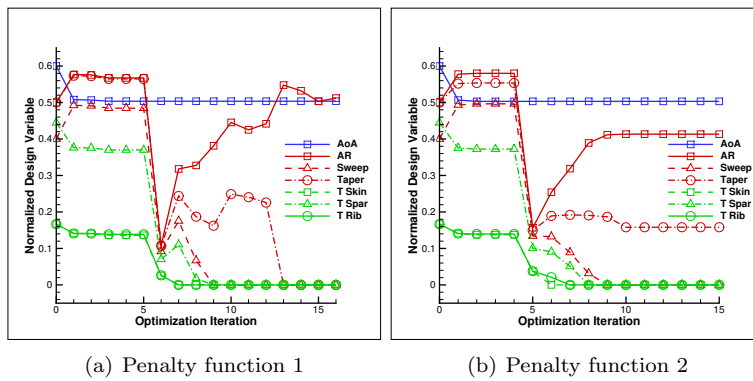


Figure 13. Design variable convergence histories.

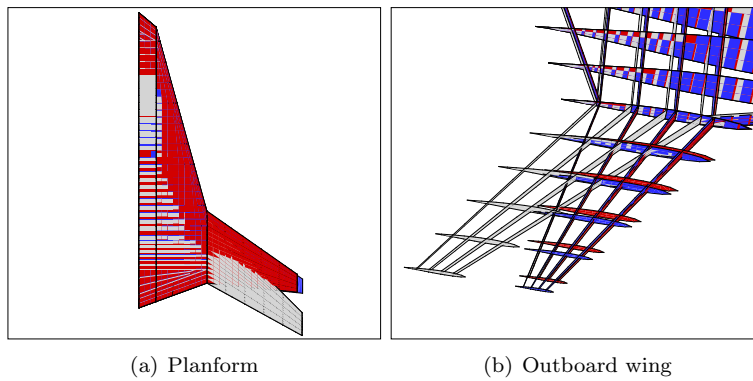


Figure 14. Comparison of final designs. Initial design is shown in gray, penalty function 1 result in blue, penalty function 2 result in red.

After the first iteration, in which the optimizer adjusts the angle of attack to satisfy the trim constraint, progress slows for several iterations. During this period of little progress, the optimizer incurs most of its expense in terms of function and gradient calls, requiring on the order of fifty calls in the first five iterations. This behavior would seem to indicate that early in the optimization, the optimizer is working on building a good approximation of the inverse Hessian so that the expected optimal points are acceptable. Once a good approximation is obtained, the optimizer rapidly reduces the penalty functions by an order of magnitude.

In both cases, the structural gauges are driven to the lower limit, with margin in the stress constraints to further lighten the structure. Thus, in future optimizations, the lower bounds may be relaxed. The sweep angle also goes to the lower bound in these cases. This is expected because the low-fidelity model does not contain an estimate of wave drag, which would drive the wing to be swept. For these cases, where only induced drag is considered, unsweeping the wing reduces weight, improving the range objective. The aspect and taper ratios between the two optimizations differ, requiring further investigation.

The number of function and gradient evaluations required in the first several iterations highlights the opportunity for multifidelity optimization to reduce cost. If the number of evaluations required using high-fidelity data is similar, replacing the line search with cheaper corrected data could produce a major cost savings.

IV. Summary and Future Work

In summary, a framework has been constructed for the multifidelity, aeroelastic analysis and optimization of air vehicles. A central aspect of this framework is the common geometric representation for each analysis discipline and fidelity. This shared source facilitates information transfer between codes and the generation of consistent analysis meshes.

Parametric studies are performed to illustrate the level of agreement (or disagreement) between analysis fidelities for aerodynamic coefficients, aeroelastic responses, and structural stresses. The studies show reasonable agreement in most cases, and in many cases may be corrected by low-order corrections used in the proposed multifidelity optimization.

Preliminary results are presented for aeroelastic optimizations with the low-fidelity model. The number of function calls in early iterations highlights the opportunity for savings by replacing high-fidelity simulations with corrected low-fidelity data.

Future work includes demonstrating the full multifidelity optimization algorithm using the analyses presented. Further work is needed to verify the accuracy and precision of finite difference sensitivities to prevent numerical difficulties in the optimizer. True analytic aeroelastic sensitivities may be introduced as they become available to avoid these issues. Finally, modification of the proposed multifidelity optimization algorithm to handle constraints directly rather than through penalty functions is a topic of future research.

Acknowledgment

This effort was funded in part by the Air Force Research Laboratory, Air Vehicles Directorate under the Civilian Academic Degree Payment (CADP) program. The authors also gratefully acknowledge the work of Dr. John Dannenhoffer, III, (Syracuse University), Mr. Bob Haimes (Massachusetts Institute of Technology), Dr. Nitin Bhagat (University of Dayton Research Institute), and Dr. Ed Alyanak (Air Force Research Laboratory) in the generation of multifidelity, multidisciplinary analysis models.

References

- ¹Love, M., Yoakum, R., and Britt, R., "Identification of Critical Flight Loads," *44th AIAA Structures, Structural Dynamics, and Materials Conference*, 2003.
- ²Council, N. R., "Pre-Milestone A and Early-Phase Systems ENgineering: A Retrospective Review and Benefits for Future Air Force Systems Acquisition," Tech. rep., National Academies Press, Washington, DC, 2008.
- ³Lewis, R. M., "A trust region framework for managing approximation models in engineering optimization," *AIAA/NASA/ISSMO Symposium on Multidisciplinary Analysis and Optimization*, 1996, pp. 1053–1055.
- ⁴Alyanak, E. and Pendleton, E., "A Design Study Employing Aeroelastic Tailoring and an Active Aeroelastic Wing Design Approach on a Tailless Lambda Wing Configuration," *AIAA Aviation*, 2014.
- ⁵Poon, N. M. K. and Martins, J. R. R. A., "An Adaptive Approach to Constraint Aggregation using Adjoint Sensitivity Analysis," *Structural and Multidisciplinary Optimization*, Vol. 34, No. 1, 2007, pp. 61–73.

- ⁶Kreisselmeier, G. and Steinhauser, R., "Systematic Control Design by Optimizing a Vector Performance Index," *IFAC Symposium on Computer Aided Design of Control Systems*, Zurich, 1979.
- ⁷Allison, D. and Alyanak, E., "Development of Installed Propulsion Performance Model for High-Performance Aircraft Conceptual Design," *15th AIAA/ISSMO Multidisciplinary Analysis and Optimization Conference*, No. June, Atlanta, GA, 2014, pp. 1–20.
- ⁸Alyanak, E., Durscher, R., Haimes, R., Dannenhoffer, J. F. I., Bhagat, N., and Allison, D., "Multi-fidelity, Gemoetry-centric Multi-disciplinary Analysis for Design," *AIAA Aviation*, AIAA, Washington, DC, 2016.
- ⁹Johnson, E. H. and Venkayya, V. B., "Automated Structural Optimization System (ASTROS)—Volume I: Theoretical Manual," Tech. rep., Air Force Wright Aeronautical Laboratories, Wright-Patterson AFB, OH, 1988.
- ¹⁰Neill, D. J., Johnson, E. H., and Herendeen, D. L., "Automated Structural Optimization System (ASTROS)—Volume II: User's Manual," Tech. rep., Air Force Wright Aeronautical Laboratories, Wright-Patterson AFB, OH, 1988.
- ¹¹Harris, J. R., "An Analysis and Correlation of Aircraft Wave Drag," Tech. rep., NASA, Hampton, VA, 1963.
- ¹²Anderson, W. K. and Bonhaus, D. L., "An Implicit Upwind Algorithm for Computing Turbulent Flows on Unstructured Grids," *Computers and Fluids*, Vol. 23, No. 1, 1994, pp. 1–21.
- ¹³Biedron, R. T., Derlaga, J. M., Gnoffo, P. A., Hammond, D. P., Jones, W. T., Kleb, B., Lee-Rausch, E. M., Nielsen, E. J., Park, M. A., Rumsey, C. L., Thomas, J. L., and Wood, W. A., "FUN3D Manual: 12.4," Tech. rep., NASA, Hampton, VA, 2014.
- ¹⁴Woodward, F. A., "An Improved Method for the Aerodynamic Analysis of Wing-Body-Tail Configurations in Subsonic and Supersonic Flow: Part I—Theory and Application," Tech. rep., NASA CR-2228, Washington, DC, 1973.
- ¹⁵Harder, R. L. and Desmarais, R. N., "Interpolation using Surface Splines," *Journal of Aircraft*, Vol. 9, No. 2, 1972.
- ¹⁶Biedron, R. T. and Thomas, J. L., "Recent Enhancements to the FUN3D Flow Solver for Moving-Mesh Applications," *47th AIAA Aerospace Sciences Meeting*, ALAA, Orlando, FL, 2009.
- ¹⁷Marcum, D. L. and Weatherill, N. P., "Unstructured Grid Generation Using Iterative Point Insertion and Local Reconnection," *AIAA Journal*, Vol. 33, No. 9, 1995, pp. 1619–1625.
- ¹⁸Marcum, D. L., "Unstructured Grid Generation Using Automated Point Insertion and Local Reconnection," *The Handbook of Grid Generation*, edited by J. F. Thompson, B. Soni, and N. P. Weatherill, CRC Press, 1998, pp. 18–1.
- ¹⁹Bryson, D. E. and Rumpfkeil, M. P., "Comparison of Unified and Sequential-Approximate Approaches to Multifidelity Optimization," *AIAA SciTech*, Grapevine, TX, 2017.
- ²⁰Bryson, D. E. and Rumpfkeil, M. P., "Variable-Fidelity Surrogate Modeling of Lambda Wing Transonic Aerodynamic Performance," *54th AIAA Aerospace Sciences Meeting*, No. January, 2016, pp. 1–19.
- ²¹Boopathy, K. and Rumpfkeil, M. P., "Unified Framework for Training Point Selection and Error Estimation for Surrogate Models," *AIAA Journal*, Vol. 53, No. 1, 2015, pp. 215–234.
- ²²Han, Z.-h., Götz, S., and Zimmermann, R., "Improving variable-fidelity surrogate modeling via gradient-enhanced kriging and a generalized hybrid bridge function," *Aerospace Science and Technology*, Vol. 25, No. 1, 2013, pp. 177–189.
- ²³Gano, S. E., Renaud, J. E., and Sanders, B., "Hybrid Variable Fidelity Optimization by Using a Kriging-Based Scaling Function," *AIAA Aviation*, Vol. 43, No. 11, 2005, pp. 2422–2430.
- ²⁴Ng, L. W. T., Huynh, D. B. P., and Willcox, K. E., "Multifidelity Uncertainty Propagation for Optimization Under Uncertainty," , No. September, 2012, pp. 1–15.
- ²⁵Fischer, C. C., Grandhi, R. V., and Beran, P. S., "Bayesian Low-Fidelity Correction Approach to Multi-Fidelity Aerospace Design," *AIAA SciTech*, No. January, American Institute of Aeronautics and Astronautics, Grapevine, TX, 2017, pp. 1–22.
- ²⁶Byrd, R. H., Lu, P., and Nocedal, J., "A Limited Memory Algorithm for Bound Constrained Optimization," *SIAM Journal on Scientific and Statistical Computing*, Vol. 16, No. 5, 1995, pp. 1190–1208.

This article has been cited by:

1. Chris M. Meckstroth. Parameterized, Multi-fidelity Aircraft Geometry and Analysis for MDAO Studies using CAPS . [[Citation](#)] [[PDF](#)] [[PDF Plus](#)]
2. Ana Garcia Garriga, Sangeeth S. Ponnusamy, Laura Mainini. A multi-fidelity framework to support the design of More-Electric Actuation . [[Citation](#)] [[PDF](#)] [[PDF Plus](#)]
3. Dean Bryson, Markus Rumpfkeil. Aeroelastic Design Optimization using a Multifidelity Quasi-Newton Method . [[Citation](#)] [[PDF](#)] [[PDF Plus](#)]
4. Dean E. Bryson, Markus P. Rumpfkeil. 2017. All-at-once approach to multifidelity polynomial chaos expansion surrogate modeling. *Aerospace Science and Technology* . [[Crossref](#)]